FEATURE ARTICLE

Photodissociation Dynamics of Small Aromatic Molecules Studied by Multimass Ion Imaging

Chi-Kung Ni,* Cheng-Ming Tseng,† Ming-Fu Lin, and Yuri A. Dyakov

Institute of Atomic and Molecular Sciences, Academia Sinica, Taipei, 10617 Taiwan

Received: June 23, 2007; In Final Form: August 10, 2007

The photodissociation dynamics of various aromatic molecules, studied using multimass ion imaging techniques, is reviewed. The experimental data reveals new isomerization and dissociation mechanisms. Our investigation of benzene, pyridine, and pyrimidine finds that H-atom elimination thresholds remain the same for the three molecules. We also notice that ring-opening dissociation thresholds decrease rapidly with the increase of the number of nitrogen atoms in the aromatic ring. Hydrogen atom elimination is the sole dissociation channel for benzene at 193 nm. Along with H-atom elimination, we observe five distinct ring-opening dissociation channels for pyridine at 193 nm. No dissociation channels were observed for benzene and pyridine at 248 nm. Ring-opening dissociation channels are the major channels for pyrimidine, which dissociates at 193 nm and also at 248 nm. A six-membered to seven-membered ring isomerization was observed for photodissociation processes involving toluene, *m*-xylene, aniline, 4-methylpyridine, α-fluorotoluene, and 4-fluorotoluene, indicating a general isomerization mechanism for all such aromatic molecules. What is significant, is that during the isomerization, atoms (i.e., carbon, nitrogen, fluorine, and hydrogen) belonging to respective alkyl or amino groups are involved in an exchange with atoms within the aromatic ring. This type of isomerization is not observed in other aromatic isomerization mechanisms. For small tyrosine chromophores, such as phenol, 4-methylphenol, and 4-ethylphenol, H-atom elimination from a repulsive excited state plays a key role. However, dissociation is quenched in large chromophores like 4-(2-aminoethyl)-phenol. Our work demonstrates the capability and high sensitivity of multimass ion imaging techniques in the study of aromatic compounds.

I. Introduction

The photochemistry of benzene and its derivatives is often exemplified in both theoretical and experimental investigations. A conspicuous feature emerging from studies of aromatic photochemistry concerns the photoexcitation of these molecules, leading to a rich variety of reactions.

The ultraviolet photodecomposition of aromatic molecules has been studied extensively in condensed and gas phases, with various products found and analyzed upon photolysis. However, in many cases, difficulties in elucidating mechanisms from product analysis are compounded by sequential collisions with background molecules in addition to complicated forms for the energy dependence of respective isomerization and dissociation channels. Fortunately, collisions with background molecules can be significantly reduced by studying these reactions using molecular beam techniques, which afford collisionless conditions. Photofragments are more easily identified, and parent molecule energies after photoexcitation remain unaltered by intermolecular energy transfer collisions. With precise control of the photon energy, the energy dependence can be clearly defined. Furthermore, detailed molecular photodissociation mechanisms can be uncovered from measurements of the dissociation rates, fragment translational energy distributions, product-state distributions, and fragment angular distributions.

Indeed, molecular photodissociation has been studied using molecular beams in tandem with a variety of experimental techniques. The state-specific detection of photodissociation products using methods such as laser-induced fluorescence, multiphoton ionization, and coherent laser scattering have provided detailed information on the dynamics of photodissociation processes. Unfortunately, many polyatomic photofragments cannot be detected by these techniques, because of the complexity of the spectra. Fortunately, photofragment translational spectroscopy using ionization detection methods is universally applicable to all products. Consequently, a variety of polyatomic molecules have been studied using this method.[1]

We have constructed a new molecular beam apparatus, from which the identification of dissociation products for many different channels along with measurements of their respective translational energies can be carried out simultaneously.[2] We employ a vacuum ultraviolet (VUV) laser to ionize photofragments, instead of traditional electron impact methods, greatly reducing background noise levels and fragment cracking upon ionization. Multimass detection capability and high sensitivity are essential in the study of polyatomic molecules, especially so for aromatic compounds. Our experimental data in conjunction with ab initio calculations of the reaction potential energy

* Corresponding author. E-mail: ckni@po.iams.sinica.edu.tw. Also located at the Department of Chemistry, National Tsing Hua University, Hsinchu, Taiwan.

† Also located at the Department of Chemistry, National Taiwan University, Taipei, Taiwan.

10.1021/jp074904j CCC: $37.00
Published on Web 10/13/2007

Chi-Kung Ni received his B.S. in Chemistry from National Tsing Hua University, Taiwan in 1985 and his Ph.D. in Physical Chemistry from Columbia University, NY in 1993. He was a postdoctoral associate in UC Berkeley (1993∼1995) before joining the Institute of Atomic and Molecular Sciences (IAMS), Academia Sinica, Taiwan. He is currently a Research Fellow in IAMS. His research includes photodissociation dynamics of organic molecules in molecular beam, energy transfer of highly vibrationally excited molecules studied by crossed-molecular beam and high-resolution molecular spectroscopy.

Cheng-Ming Tseng received his B.S. and M.S. from National Taiwan University, Taiwan in 2000 and 2002, respectively. He is currently a research assistant in the Institute of Atomic and Molecular Sciences (IAMS), Academia Sinica, and pursuing his doctoral degree in physical chemistry at National Taiwan University. His future research interests include the application of novel technologies in biophysical chemistry.

surfaces reveals new isomerization and dissociation mechanisms. This article reviews the photodissociation dynamics of small aromatic molecules using our new method. We focus on several groups of molecules. Within each group, both the similarities and the differences in the photodissociation dynamics are discussed.

II. Experimental Method

The multimass ion imaging techniques we use have been described in detail elsewhere.[2−4] Here, we provide a brief description. Figure 1 is a schematic diagram of the apparatus. An ultraviolet laser pulse photodissociates molecules in the molecular beam. Because of the recoil velocity of the dissociation products and the center-of-mass velocity (i.e., the molecular beam velocity), fragments are distributed within an expanding sphere on flight to the ionization region, where they are photoionized by a VUV laser pulse. The time delay between UV photolysis laser and VUV laser pulses was sufficiently long (5−120 μs) such that the diameter of the fragment sphere reached from 1 to 8 cm before ionization. The diameter of the expanding sphere was significantly larger than that of the VUV

Ming-Fu Lin received his B.S. in Chemistry from National Taiwan Normal University, in 2001 and his M.S. in Chemistry from National Taiwan University in 2003. He is currently a research assistant in the Institute of Atomic and Molecular Sciences (IAMS), Academia Sinica, Taiwan. He is going to pursue his doctoral degree in Physical Chemistry at UC Berkeley in Spring 2008.

Yuri A. Dyakov received his M.S. in Physics from Kazan State University, Russia in 1992 and his Ph.D. in Physics from Karpov Institute of Physical Chemistry in 2000. He is currently a postdoctoral fellow in IAMS, Academia Sinica, Taiwan. His research interests include quantum chemistry calculation.

laser beam (<0.5 mm) at the time the pulse arrived. The distance and time delay between the UV photolysis laser and the VUV laser pulses were set so that the time delay matched with the velocity of the molecular beam. This ensured that the VUV laser beam passed through the center of the expanding photofragment sphere, thus, generating photofragment ions along the VUV beam path via photoionization. Although there are fragment ions of different masses along the VUV beam path (in accord with the various photodissociation products), each fragment ion has its own intensity distribution along this path. The length of a respective distribution is proportional to the fragment recoil velocity in the center-of-mass frame multiplied by the delay time.

A pulsed electric field is used to extract ions generated by the VUV laser pulse and into a mass spectrometer for separation of the different masses. The entrance to the mass spectrometer is a long slit parallel to the VUV laser beam in order to accept ions produced at various positions along the VUV laser beam path. Our mass spectrometer is essentially a radial cylindrical energy analyzer. The ion extraction field for the energy analyzer was turned on several nanoseconds after the arrival of the VUV laser pulse and turned off before ions left the extraction region and entered the energy analyzer. The momentum p, of the ions obtained from the pulsed field is given by $p = \int F\,dt = \int q \times E\,dt$: where, F is the force, q is the charge of ion, and E is the

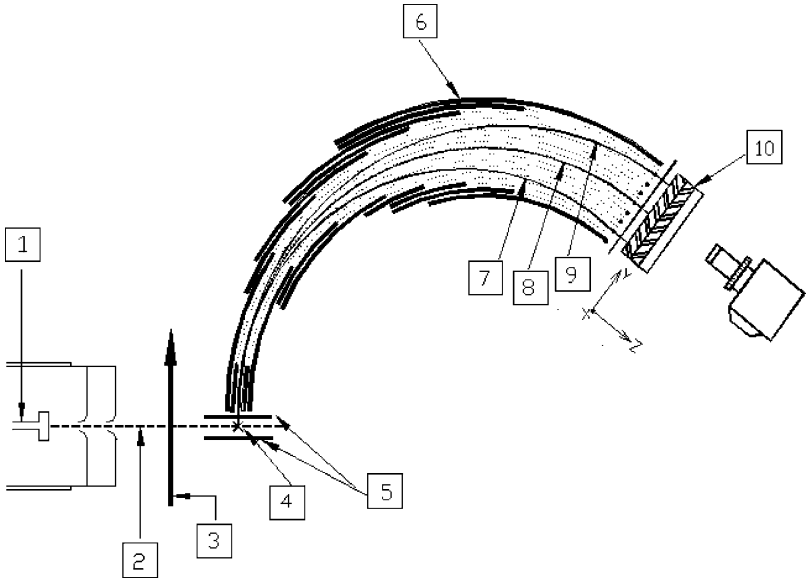

Figure 1. Schematic diagram of the multimass ion imaging system. (1) Nozzle, (2) molecular beam, (3) photolysis laser beam, (4) VUV laser beam, which was perpendicular to the plane of the paper, (5) ion extraction plates, (6) energy analyzer (7−9) simulation ion trajectories of m/e = 16, 14, and 12, respectively, and (10) two-dimensional detector, where the Y axis is the mass axis and the X axis (perpendicular to the plane of the paper) is the velocity axis.

electric field. The time t range in the integral is the electric field duration. The equation shows that the momentum is independent of mass. Consequently, all ions are accelerated to the same linear momentum along the direction of the electric field. Therefore, a fragment ion's translational energy resulting from the pulsed electric field is proportional to the reciprocal of the fragment's mass. Photofragment ions entering the cylindrical energy analyzer can then be separated according to differences in translational energies as obtained from the pulsed electric field. Note that the VUV laser beam passed through the center of the fragment sphere. Fragments ionized by the VUV laser had a recoil velocity only in the direction of the VUV laser beam path. These recoil velocities were perpendicular to both of the electric fields in the extraction region and inside the energy analyzer and were not affected by these fields. During the flight through the mass spectrometer, the length of fragment ions' distribution kept expanding according to the fragment recoil velocity. Meanwhile, ions of different masses started separating from each other in the energy analyzer in accordance with the energy they have obtained from the extraction field. Trajectories for different masses are illustrated in Figure 1. At the exit port of the mass spectrometer, a two-dimensional (2-D) ion detector is used to detect ion positions and intensity distributions. As illustrated by Figure 1, within the detector, the X axis represents the recoil velocity axis, and the Y axis represents the mass axis. Velocity distributions in the center-of-mass frame for many different fragments were obtained simultaneously from the position and intensity distributions of the image. A typical image is shown by Figure 2a,b. Photofragment translational energy distributions (useful as we will explain in the determination of the dissociation mechanism) can be calculated directly from the velocity distributions. Additionally, in adherence with the conservation of linear momentum in the center-of-mass frame, a fragment's linear momentum as obtained from the velocity distribution can be used to confirm fragment partners in respective dissociation channels. This is particularly important when fragment cracking occurs upon ionization.

If the dissociation rate is small, some excited molecules will not dissociate immediately after absorption of UV photolysis photons. Those molecules containing large internal energies stay within the molecular beam. When they reach the ionization region where they are ionized by the VUV laser, the result is that parent molecules dissociate into fragment right after ionization (dissociative ionization as shown by reaction 4). Because dissociation and ionization occur at the same position, the image from dissociative ionization is a 2-D projection of the photofragment ion's three-dimensional (3-D) recoil velocity distribution. It is a disk-like image, unlike the line-shape images obtained from the dissociation of neutral molecules (as shown by reactions 2 and 3). With the VUV laser's position fixed, only the intensity of the disk-like image changes with the delay time between two laser pulses. The size of the disk-like image did not change with the delay time. Therefore, ion images resulting from dissociative ionization can be distinguished from images resulting from dissociation products of neutral molecules

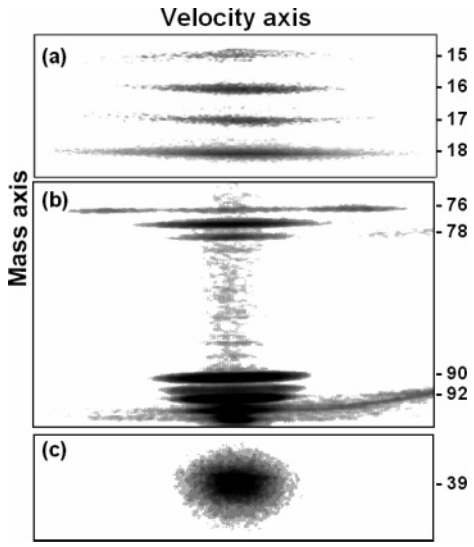

Figure 2. Photofragment ion images of (a) CH_3 (m/e = 15), CH_2D (m/e = 16), CHD_2 (m/e = 17), and CD_3 (m/e = 18) from photodissociation of d_3-toluene; (b) C_6H_4 (m/e = 76), C_6H_5 (m/e = 77), C_5NH_4 (m/e = 78), C_6H_5N (m/e = 91), and C_6H_5NH (m/e = 92) from photodissociation of aniline; and (c) C_3H_3 (m/e = 39) from photodissociation of pyridine.

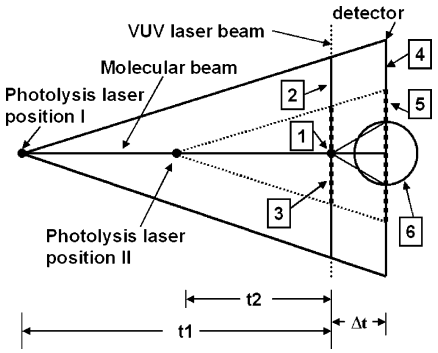

Figure 3. Relationship between the lengths of the line shape images, resulting from different photolysis laser positions and the disk-like image from the dissociative ionization. [1] represents the crossing point for the molecular beam and the VUV laser beam, where dissociative ionization occurs. [2] and [3] represent the lengths of the fragment ion segment created by the VUV laser photoionization from two different photolysis laser positions. [4] and [5] represent the lengths of the fragment ion image on the detector from two different photolysis laser positions. [6] represents the disk-like image. t_1 and t_2 give the two different delay times between the photolysis laser pulse and the VUV laser pulse. Δt is the flight time in the mass spectrometer.

by the shape of the image as well as the change in delay time. A typical disk-like image is also shown in Figure 2c.

$$A + h\nu_{UV} \rightarrow A^* \quad \text{(excitation)} \tag{1}$$

$$A^* \rightarrow B + C \quad \text{(dissociation)} \tag{2}$$

$$B + h\nu_{VUV} \rightarrow B^+ + e^-; \quad C + h\nu_{VUV} \rightarrow C^+ + e^- \quad \text{(fragment ionization)} \tag{3}$$

$$A^* + h\nu_{VUV} \rightarrow D^+ + E + e^- \quad \text{(dissociative ionization)} \tag{4}$$

The relationship between the length of the line-shape images, that of the disk-like images, and the positions of the UV and VUV laser beams are shown in Figure 3.

In addition to photofragment translational energies, information concerning dissociation rates is obtained from product growth or the decay of excited parent molecules with respect to the delay time between pump and probe laser pulses. For some molecules, the mass-to-charge ratio *m*/*e* for the ion from dissociative ionization is identical to that from dissociation (reactions 2 and 3). The measurement is, therefore, a combination of product growth and parent decay. Accurate measurements can be obtained, however, only when the dissociation rate is sufficiently large that most of the molecules have dissociated into fragments before molecular beam particles and fragments have left the detection region. This method is particularly useful for dissociation rates ranging from 5×10^7 s^{-1} (as limited by laser pulse duration) to 10^6 s^{-1}. When dissociation rates are too low, the methods just described cannot be applied. In this case, dissociation rates can be obtained from intensity changes in the disk-like images at various delay times (at various UV photolysis laser positions along the molecular beam). Dissociation rates as low as 5×10^3 s^{-1} can be measured using this method. Dissociation rates can also be measured from line-shape image intensity distributions. Because line-shape image intensities result from the accumulation of products produced during the period between pump and probe laser pulses, the ion image intensity distribution is a function of both the fragment recoil velocity distribution and the dissociation rate. With our instrumentation, image intensity profiles are sensitive to dissociation rates in the region of 2×10^4 to 10^5 s^{-1}.

III. Results and Discussion

A. Benzene, Pyridine, and Pyrimidine. *Benzene.* Photodecomposition of benzene, the simplest aromatic molecule, has been studied extensively. The primary photoproducts of benzene vapor at 184.9 nm are an isomer of benzene,[5,6] later identified as fulvene,[7,8] and polymers. *Cis*- and *trans*-1,3-hexadien-5-yne[9,10] along with small amounts of methane, ethane, ethylene, hydrogen, and acetylene were also observed.[5,11] Two other isomers, benzvalene and Dewar benzene, were obtained, however, only in condensed phase. The photodissociation of benzene at 193 and 248 nm has been investigated in a molecular beam.[12] In addition to both H-atom and H_2 elimination, a ring-opening dissociation channel ($C_6H_6 \rightarrow C_5H_3 + CH_3$) was observed. Branching ratios for these three channels were reported as 0.8, 0.16, and 0.04, respectively. However, a recent ab initio calculation,[13−15] as illustrated in Figure 4, showed that the dissociation barrier for the ring-opening channel is close to the 193 nm photon energy. As a consequence, the branching ratio for the ring-opening channel is expected to be negligible.

Despite extensive studies, only recently has the controversy over the photodissociation channels appearred to have been settled. Our experimental data demonstrates that H-atom elimination is the only one-photon dissociation channel for benzene at 193 nm.[16,17] The translational energy distribution is small with probability decreasing monotonically with energy. These characteristics are typical for dissociation from the ground electronic state with no exit barrier. A dissociation rate of $1 \pm 0.2 \times 10^5$ s^{-1} (as illustrated in Figure 5), which corresponds to a lifetime $\tau = 10 \pm 3$ μs, was obtained at 193 nm excitation. This is close to the dissociation rate, 8.9×10^4 s^{-1}, obtained when using the Rice−Ramsperger−Kassel−Marcus (RRKM) model on the ground electronic state surface.[15] However, no fragment was observed at 248 nm. The dissociation rate for benzene excited by 248 nm photons is too small to be accurately measured. It is estimated to be smaller than 3×10^3 s^{-1}, as illustrated in Figure 5.

Ring-opening channels, such as $C_6H_6 \rightarrow C_5H_3 + CH_3$ and $C_6H_6 \rightarrow C_4H_3 + C_2H_3$ (along with many others) were observed and confirmed by momentum matching between heavy and light fragments within each channel. However, UV photolysis laser intensity as low as 1.2 mJ/cm^2 was used in the experiment and showed that all ring-opening dissociation channels are from two-photon dissociation.[17] This supports the potential energy surfaces derived from ab initio calculations.

Pyridine. Photolysis of pyridine in the UV region produced H_2, C_2H_2, HCN, C_2H_4, and a brown deposit.[18,19] The photodissociation of pyridine in a molecular beam has been investigated at 193 nm. Hydrogen-atom elimination as well as three distinct ring-opening dissociation channels have been reported.[20] In order to determine the photolysis photon-number-dependence for these ring-opening dissociation channels, laser intensities in the range 0.131−7.84 mJ/cm^2 (approximately 100 times smaller than the laser intensities used in a previous study) were used in our investigation.[21] At 193 nm, the absorption cross section for pyridine is 1.5×10^{-17} cm^2.[22] Consequently, the UV photolysis laser intensity we used in this experiment did not saturate the transition. After absorption of one photon (193 nm), the absorption cross section for a second photon may change. Unless the second photon absorption cross section increases by a factor of 1000 and becomes abnormally as large as 10^{-14} cm^2, the second photon absorption will not be saturated at such a low

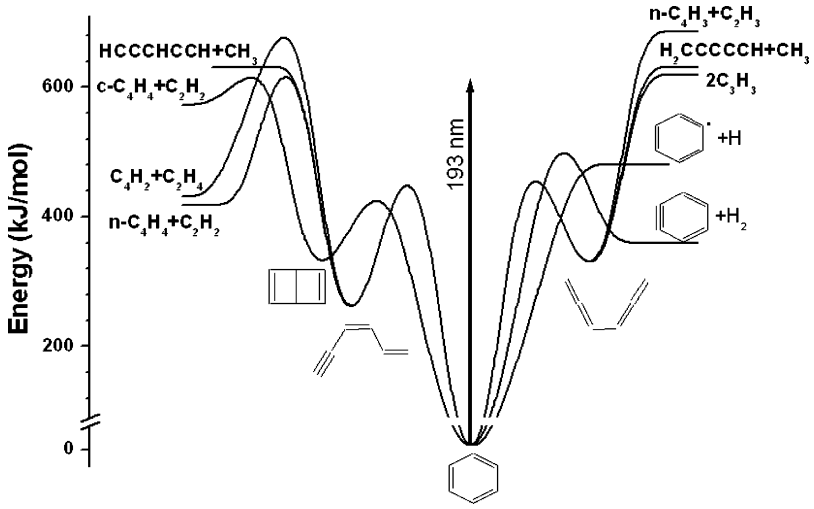

Figure 4. Simplified potential energy diagram for various isomerization and dissociation channels of benzene. Note that all ring-opening dissociation channels have thresholds or barrier heights close to the 193 nm photon energy.

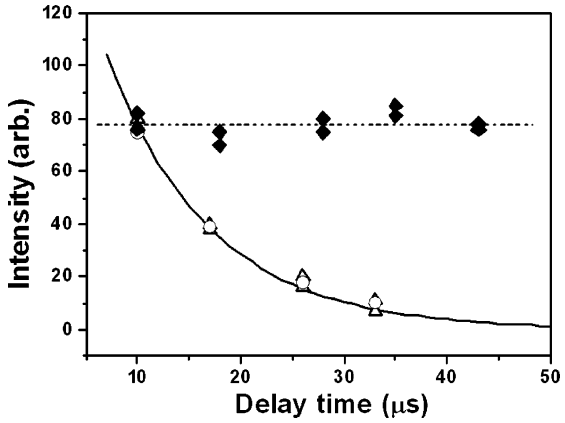

Figure 5. Changes in the disk-like image intensity for mass-to-charge ratio $m/e = 52(\triangle)$, $39(\bigcirc)$, as a function of delay time from the dissociative ionization of hot C_6H_6 after 193 nm excitation. The solid line gives the fit corresponding to a lifetime $\tau = 9.5$ μs. The solid diamonds (◆) represent the disk-like imaging intensity change for $m/e = 52$ from hot C_6H_6 after 248 nm excitation. The dashed line (---) represents no intensity changes for $m/e = 52$ with delay time.

photolysis laser intensity, either. Therefore, the dependence of the photofragment ion intensities on the number of photolysis photons can be determined. Our experimental data reveals 6 dissociation channels from 1-photon dissociation at 193 nm:

$$C_5NH_5 \rightarrow C_5NH_4 + H \quad (5)$$

$$C_5NH_5 \rightarrow C_4H_4 + HCN \quad (6)$$

$$C_5NH_5 \rightarrow C_4NH_2 + CH_3 \quad (7)$$

$$C_5NH_5 \rightarrow C_3NH + C_2H_4 \quad (8)$$

$$C_5NH_5 \rightarrow C_2NH_2 + C_3H_3 \quad (9)$$

$$C_5NH_5 \rightarrow C_2H_2 + C_3NH_3 \quad (10)$$

The same dissociation rate constant, $k = 7.7 \times 10^6$ s^{-1}, was obtained from the growths of various dissociation products and the decay of excited pyridine (as shown in Figure 6) indicating that all reactions occur on the same electronic state. The fragment translational energy distributions are shown in Figure 7. There are two types of behavior. Distributions exhibiting a peak close to zero and probability decreasing monotonically with

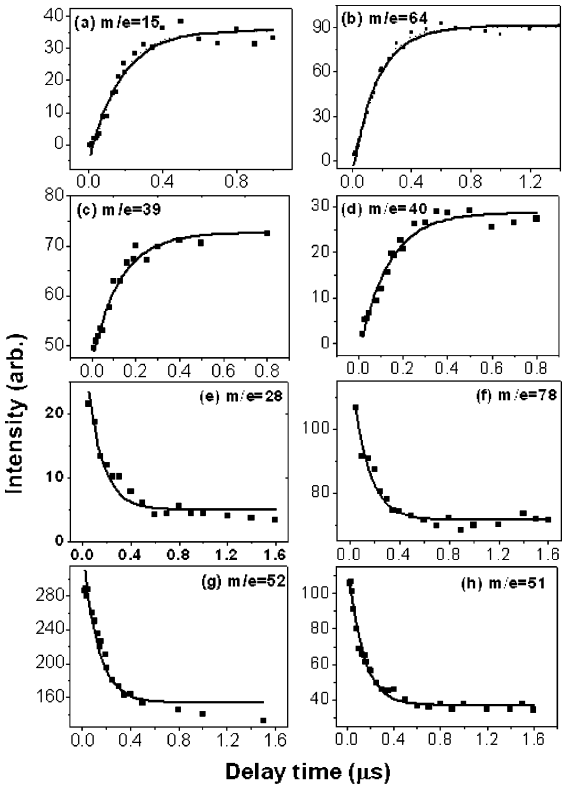

Figure 6. Intensity changes of the disk-like images and product growth with respect to the delay time between pump and probe laser pulses. The solid squares are the experimental data. Solid lines are the fit to A $\times$ exp($-kt$) + B $\times$ (1 $-$ exp($-kt$)) where k represents the dissociation rate.

increasing translational energy are typical characteristics of dissociation from a molecule undergoing internal conversion to the lower electronic state with no exit barrier. This type of behavior is found for dissociation channels generating two radicals. By contrast, distributions showing their peak at large average translational energies are dissociation from a repulsive excited state or dissociation from an electronic state with a large exit barrier. This type of distribution was found for dissociation channels generating two closed-shell molecules. One possible electronic state to which all of the dissociation reactions evolve is the ground electronic state. This is a reasonable assumption because the ground state potential is not expected to feature an exit barrier when the dissociation products are two radicals.

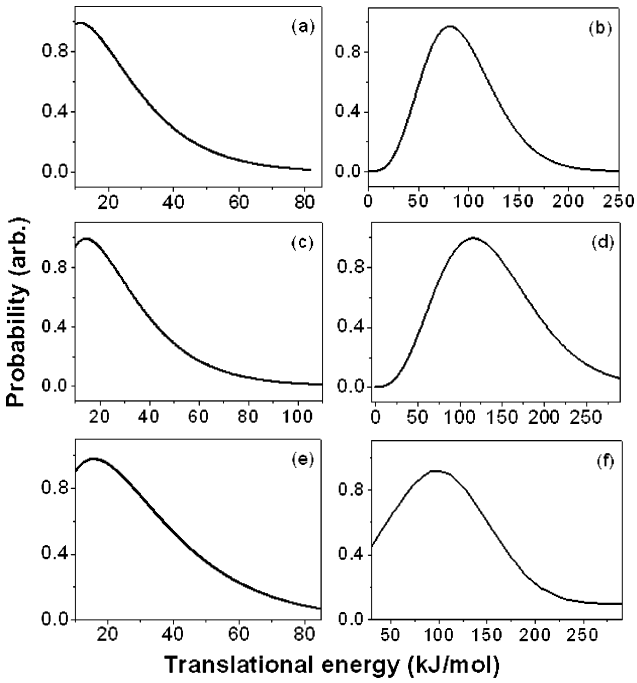

Figure 7. Translational energy distributions for the reactions (a) $C_5NH_5 \rightarrow C_4NH_2 + CH_3$, (b) $C_5NH_5 \rightarrow C_3NH + C_2H_4$, (c) $C_5NH_5 \rightarrow C_2NH_2 + C_3H_3$, (d) $C_5NH_5 \rightarrow C_4H_4 + HCN$, (e) $C_5NH_5 \rightarrow C_5NH_4 + H$, and (f) $C_5NH_5 \rightarrow C_3NH_3 + C_2H_2$.

Additionally, the ground state potential is expected to have a large exit barrier when the products are two closed-shell molecules. These properties of the ground electronic state potential energy surface are confirmed by ab initio calculations (see Figure 8). Indeed, the fragment translational energy distributions of reactions $C_5NH_5 \rightarrow C_3NH + C_2H_4$ and $C_5NH_5 \rightarrow C_4H_4 + HCN$ show that the maximum translational energies reach the maximum available energies for these reactions. Because the maximum translational energy corresponds to products produced in the ground electronic state and also that the ground states of these closed-shell fragments correlate solely with the ground state of the parent molecule, dissociation should occur in the ground electronic state. As a result, we conclude that reactions 5−10 occur on the ground electronic state potential. For 248 nm photoexcitation, the dissociation rate is too slow (estimated to be smaller than 2×10^3 s^{-1}) to produce any measurable fragment in our experimental observation window.

Fragments with different numbers of deuterium (D) atoms were observed from the photodissociation of 2,6-d_2-pyridine at 193 nm. The respective ratios between various D-atom-substituted fragments from experimental measurement are very close to the statistical values. This suggests that the isotopic scrambling between D and H atoms in 2,6-d_2-pyridine is nearly complete before dissociation occurs.

Although the final dissociation process occurs on the ground electronic state, the isomerization of pyridine in the excited electronic state before internal conversion to the ground state cannot be totally excluded. One possible structural change in the excited electronic state concerns ring permutation, which is one of the most important isomerizations of aromatic molecules in the S_1 state.[23−26] Because of the lack of potential energy surfaces for electronically excited states, only the ground state potential energy surface is discussed here. Potential energy surfaces from ab initio calculations for various isomerization and dissociation pathways are illustrated in Figure 8. The hydrogen-to-deuterium (H/D) exchange occurs on the ground electronic state via H/D migration around the aromatic ring or through ring permutation. The elimination of hydrogen can occur directly from the six-membered ring structure. On the other hand, ring-opening dissociation channels require extensive isomerization before dissociation occurs. Most of these isomerizations involve the change from a ring to a linear structure. The isomerizations also provide additional H/D exchange. All of the ring-opening channels have more than one isomerization pathway, and some of them have products with multiple structures. The potential energy diagram (Figure 8) also illustrates that the isomerization barriers, and dissociation thresholds are all significantly smaller than the 193 nm photon energy.

Pyrimidine. Pyrimidine maintains similar photophysical properties to those of benzene and pyridine. However, few photodissociation studies involving pyrimidine have been conducted. Our results find the dissociation rates to be $>5 \times 10^7$ s^{-1} and 1×10^6 s^{-1} at 193 and 248 nm, respectively.[27] Six dissociation channels were observed in the photodissociation of pyrimidine at 193 nm.

$$C_4N_2H_4 \rightarrow C_4N_2H_3 + H \quad (11)$$

$$C_4N_2H_4 \rightarrow C_3NH_3 + HCN \text{ (or HNC) or } C_2H_2 + 2HCN \quad (12)$$

$$C_4N_2H_4 \rightarrow 2C_2NH_2 \quad (13)$$

$$C_4N_2H_4 \rightarrow CH_3N + HC_3N \quad (14)$$

$$C_4N_2H_4 \rightarrow C_4NH_2 + NH_2 \quad (15)$$

$$C_4N_2H_4 \rightarrow CH_2N + C_3NH_2 \quad (16)$$

Only reactions 11−14 were observed at 248 nm.

Dissociation properties (translational energy distributions and dissociation rates) for pyrimidine were found to be similar to those for pyridine, suggesting that dissociation occurs in the ground electronic state after internal conversion.

Ab initio calculations of the ground state potential energy surface show that most of the barrier heights for these channels are much lower than the analogous channels for benzene and pyridine, as illustrated in Figure 9. Low barrier heights explain the observation for the fast dissociation rate at 193 nm as well as some of the channels being open at 248 nm. As with pyridine, all of the ring-opening channels for pyrimidine require extensive isomerization before dissociation.

A comparison of benzene, pyridine, and pyrimidine finds the N-atom number dependence of the dissociation properties. The H-atom elimination thresholds are about the same for benzene, pyridine, and pyrimidine: as high as about 460 kJ/mol. However, the ring-opening dissociation barrier heights and thresholds depend strongly on the N-atom number in the aromatic ring. As the N-atom number increases from benzene to pyrimidine, the corresponding ring-opening dissociation barrier heights and thresholds decrease rapidly. For example, the dissociation threshold for $C_6H_6 \rightarrow 2C_3H_3$ is as large as 623 kJ/mol, which is close to the 193 nm photon energy. However, dissociation thresholds for analogous reactions with pyridine $C_5NH_5 \rightarrow C_3H_3 + C_2NH_2$ and pyrimidine $C_4N_2H_4 \rightarrow 2C_2NH_2$ are only 460 and 422 kJ/mol, respectively. Similar trends were found for all analogous ring-opening dissociation reactions. As a result, the dissociation rate constants at 193 nm increase from 1×10^5 s^{-1} for benzene and 7.7×10^6 s^{-1} for pyridine to $>5 \times 10^7$ s^{-1} for pyrimidine. Rate constants at 248 nm increase from a value smaller than 2×10^3 s^{-1} for benzene and pyridine

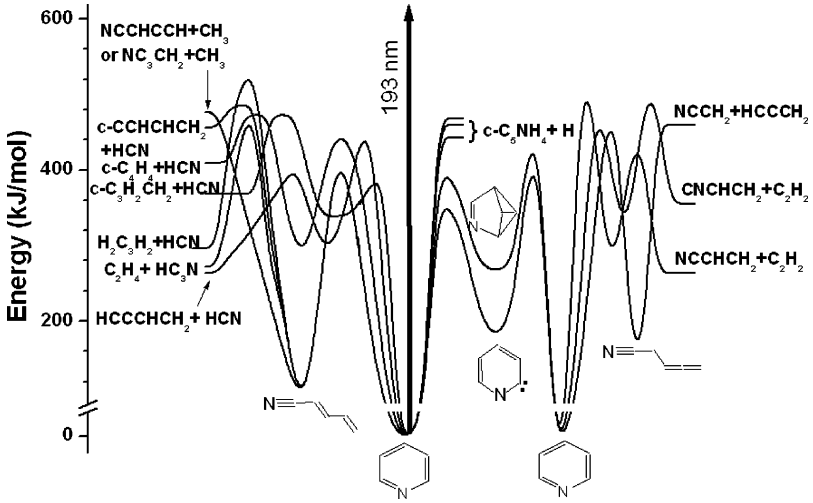

Figure 8. Simplified potential energy diagram for various isomerization and dissociation channels of pyridine.

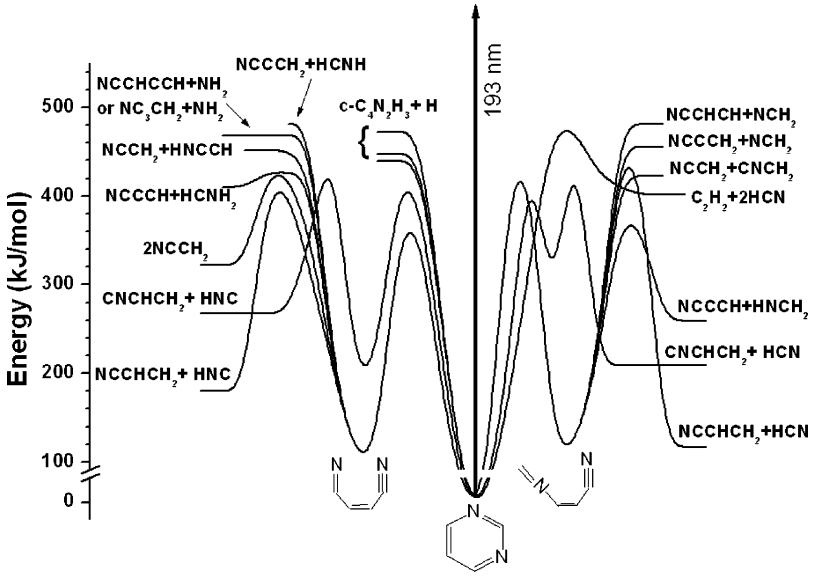

Figure 9. Simplified potential energy diagram for various isomerization and dissociation channels of pyrimidine.

to 1×10^6 s^{-1} for pyrimidine. From this, we conclude that benzene is more stable than pyridine and pyrimidine under UV irradiation and that pyrimidine is easier to decompose into fragments under similar conditions.

B. Toluene, *m*-Xylene, Methylpyridine, Aniline, 4-Fluorotoluene, and α-Fluorotoluene. *Ring Permutation.* Ultraviolet fluorescence quantum yields of alkyl-substituted benzenes in the S_1 state decrease rapidly with increasing photon energy. Fluorescence from the S_n ($n \geq 2$) states is very small.[28] For these molecules, a common unimolecular process is isomerization. Photoisomerization and subsequent formation of derivatives of fulvenes, benzvalenes, Dewar benzenes, and prismanes, for example, as well as isomerization with a change of the alkyl substitute's position in the aromatic ring after excitation to the S_1 state, have been well-characterized.[29−32] The generally accepted view is that photoisomerization of this type proceeds via formation of intermediary isomers like fulvene, benzvalene, and Dewar benzene along with their further rearomatization. It has been suggested that all isomerization processes of benzene and its alkyl derivatives can be described in terms of ring permutation.[33] Figure 10 shows some of the ring permutations of benzene and xylene. One important characteristic of ring permutation is that carbon and hydrogen atoms belonging to the alkyl group are not involved in an exchange with atoms in the aromatic ring. Ring permutation has been observed in benzene and alkyl-substituted benzene in both condensed and gas phases after excitation to the S_1 state.[34−35] Ring permutations

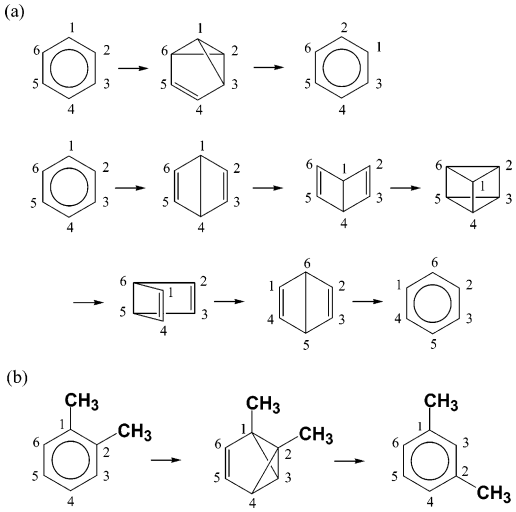

Figure 10. Some isomerization pathways of benzene and xylene through ring permutation.

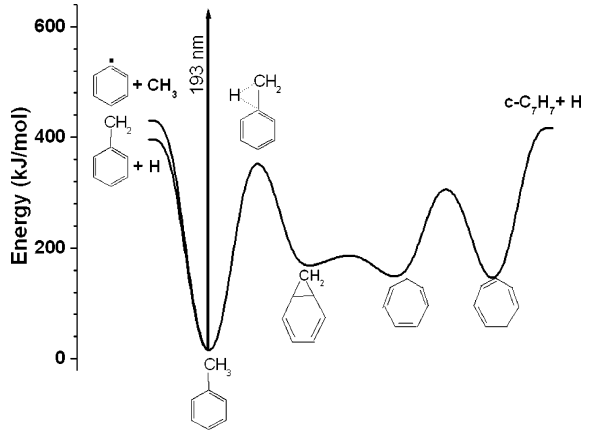

Figure 11. Simplified potential energy diagram for isomerization and dissociation channels of toluene.

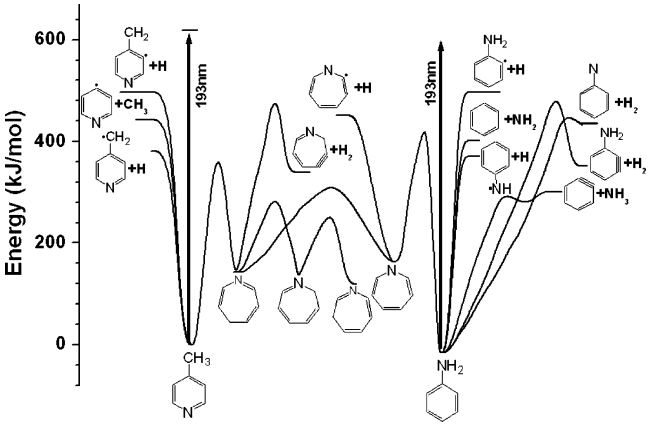

Figure 12. Simplified potential energy diagram for various isomerization and dissociation channels of aniline and 4-methylpyridine.

have also been used to describe isomerization of nitrogen-containing heterocyclic aromatic molecules.[23−25]

Under collisionless conditions, molecular energy is preserved (with the exception of deactivation by photon emission), and excited molecules will not be deactivated and stabilized through isomerization. If the initial photon energy is greater than the dissociation threshold and photon emission is absent, excited molecules will eventually dissociate into fragments. However, dissociation rates and channels after isomerization can be very different than that before isomerization.

Toluene and m-Xylene. The photodissociation of toluene and xylene after 193 nm excitation and under collisionless conditions has been studied extensively. The results were interpreted as direct C−H or C−C bond cleavage after internal conversion to the ground electronic state.[36−42] Our study of $C_6H_5CD_3$ photodissociation reveals new isomerization and dissociation mechanisms.[43] Photodissociation of d_3-toluene at 193 nm in a molecular beam shows that in addition to the major dissociation fragments, $C_6H_5CD_2$, C_6H_5, and CD_3 from the dissociation of $C_6H_5CD_3 \rightarrow C_6H_5CD_2 + D$ and $C_6H_5CD_3 \rightarrow C_6H_5 + CD_3$, heavy fragments ($C_7H_4D_3$, C_6H_4D, $C_6H_3D_2$, and $C_6H_2D_3$), and corresponding light fragment partners (CD_2H, CDH_2, and CH_3) were also observed. This suggests the existence of another dissociation channel (i.e., isotope exchange prior to dissociation). The translational energy distributions measured from various isotope-substituted fragments were found to be very similar, indicating dissociation from the same potential energy surface. Photodissociation of $C_6H_5{}^{13}CH_3$ was also studied. In addition to the major dissociation channel, $C_6H_5{}^{13}CD_3 \rightarrow C_6H_5 + {}^{13}CH_3$, the observation of $^{13}CC_5H_5$ and CH_3 indicates that the methyl-carbon atom is also involved in an exchange with aromatic carbon atoms prior to dissociation.

The experimental results cannot be adequately explained by ring permutation. They have been interpreted as the isomerization from a six-membered ring (toluene) to a seven-membered ring (cycloheptatriene) in the electronic ground state. After isomerization to the seven-membered ring, isotopic scrambling of H/D and carbon atoms occurs via H or D atom migration around the seven-membered ring. In the end, the rearomatization of cycloheptatriene to toluene with subsequent dissociation through C−C bond cleavage results in the formation of various isotope-substituted fragments. Figure 11 shows the potential energy diagram for various dissociation and isomerization pathways. The significance of this isomerization is that carbon and hydrogen atoms of the alkyl group are involved in an exchange with atoms in the aromatic ring. This kind of isomerization cannot be achieved by ring permutation.

Similarly, H and D atom exchange prior to dissociation was also observed in the photodissociation of d_6-*m*-xylene at 193 nm under collisionless conditions.[44] This particular isomerization mechanism for toluene can also be used to explain the observations concerning d_6-*m*-xylene. Isomer energies and the various transition states along isomerization pathways are very similar to those for toluene.

No photofragments were observed for toluene or *m*-xylene at 248 nm. The dissociation rates were too slow ($<3 \times 10^3$ s^{-1}) to produce fragments within our time window.

4-Methylpyridine and Aniline. Our experimental results[45] show that the major dissociation channels for 4-methylpyridine at 193 nm are $C_5NH_4CH_3 \rightarrow C_5NH_4CH_2 + H$ and $C_5NH_4CH_3 \rightarrow C_5NH_4 + CH_3$. Minor dissociation channels are $C_5NH_4CH_3 \rightarrow C_6H_5 + NH_2$ and $C_5NH_4CH_3 \rightarrow C_6H_4 + NH_3$. Additionally, a minor amount of ring-opening dissociation (e.g., HCN elimination) was observed. For aniline, the major dissociation channels are as follows: (1) $C_6H_5NH_2 \rightarrow C_6H_5NH + H$, (2) $C_6H_5NH_2 \rightarrow C_6NH_5 + H_2$, (3) $C_6H_5NH_2 \rightarrow C_6H_5 + NH_2$, and (4) $C_6H_5NH_2 \rightarrow C_6H_4 + NH_3$. A minor channel is $C_6H_5NH_2 \rightarrow C_5NH_4 + CH_3$ along with a small amount of HCN elimination. Except for H-atom elimination from aniline ($C_6H_5NH_2 \rightarrow C_6H_5NH + H$), the dissociation rates and photofragment translational energy distributions for aniline and 4-methylpyridine indicate that all other dissociation channels occur on the ground electronic state. The translational energy distribution for $C_6H_5NH_2 \rightarrow C_6H_5NH + H$ features two components: (1) a fast component resulting from dissociation of the excited-state with a repulsive potential, and (2) a slow component, resulting from dissociation on the ground electronic state. Hydrogen atom elimination from a repulsive state of the amino group has been observed in a variety of small amino-group containing molecules.[46−48]

Isomerization between aniline and 4-methylpyridine can occur via a six-membered to seven-membered ring isomerization, and its occurrence prior to dissociation can be found from the dissociation channels for the two molecules. The minor channels involving 4-methylpyridine are major channels for aniline, and the major channels for 4-methylpyridine are minor channels for aniline. This suggests that some 4-methylpyridine molecules isomerize to aniline and vice versa through the six-membered to seven-membered ring isomerization prior to dissociation. The isomerization was further confirmed in a study of the isotope-substituted compounds d_3-4-methylpyridine and d_5-aniline.

The isomer energies and transition states along isomerization and dissociation paths derived from ab initio calculations are shown in Figure 12. The isomerization of 4-methylpyridine to

a seven-membered ring initiates with a hydrogen atom shift from the methyl group to an adjacent carbon atom, followed by formation of a bicyclo-isomer intermediate and finally to a seven-membered ring structure. The energy barrier for the six-membered to seven-membered ring isomerization is comparable to the dissociation threshold for C−C and C−H bond cleavage. Although the majority of 4-methylpyridine molecules dissociate directly through C−C and C−H bond cleavage (after internal conversion), experiment shows that at least 10% of the 4-methylpyridine molecules isomerize to a seven-membered ring prior to dissociation. Dissociation and isomerization barrier heights in the ground electronic state of aniline are similar to that for 4-methylpyridine. Nearly 23% of the aniline isomerizes to a seven-membered ring prior to dissociation.

α-*Fluorotoluene and 4-Fluorotoluene.* Dissociation channels for 4-fluorotoluene at 193 nm include two major channels ($C_6H_4FCH_3 \rightarrow C_6H_4FCH_2 + H$ and $C_6H_4FCH_3 \rightarrow C_6H_4F + CH_3$) and two minor channels ($C_6H_4FCH_3 \rightarrow C_6H_5CH_2$ [or C_7H_7] + F and $C_6H_4FCH_3 \rightarrow C_6H_5CH$ [or C_7H_6] + HF).[49] Absorption of 193 nm photons corresponds to excitation of the aromatic ring, which is a stable state with respect to dissociation. Consequently, dissociation must occur after internal conversion or via intersystem crossing to a lower electronic state. The dissociation rate was found to be 1.0×10^6 s^{-1}. A slow dissociation rate and small translational energy release suggest dissociation on the ground electronic state after internal conversion. The major channels are analogous to the H-atom and CH_3 elimination channels of toluene. Both reactions have low dissociation thresholds and are expected to occur at this photon energy. Conversely, F-atom elimination is not likely to occur since the C−F bond energy is large. Furthermore, the peak in the translational energy distribution for HF elimination from 4-fluorotoluene is close to zero. This is very different from the large translational energy release of HF elimination from fluorobenzene, suggesting that the HF elimination mechanism of 4-fluorotoluene must differ from that of fluorobenzene.[50,51]

Four dissociation channels were observed for α-fluorotoluene at both 193 and 248 nm, including 2 major channels ($C_6H_5CH_2F \rightarrow C_6H_5CH_2$ [or C_7H_7] + F and $C_6H_5CH_2F \rightarrow C_6H_5CH$ [or C_7H_6] + HF) and 2 minor channels ($C_6H_5CH_2F \rightarrow C_6H_5CHF$ + H, $C_6H_5CH_2F \rightarrow C_6H_5 + CH_2F$).[49] The respective dissociation rates for α-fluorotoluene at 193 and 248 nm are 3.3×10^7 and 5.6×10^5 s^{-1}. The minor channels are anticipated because of similarities between toluene and α-fluorotoluene; however, the major channels are not nearly as predictable. Additionally, the translational energy distributions for the F and HF elimination channels are similar to those of 4-fluorotoluene.

Because α-$C_6H_5CH_2F$ and 4-$C_6H_4FCH_3$ have similar translational energy distributions in F and HF elimination channels, it is likely that both α-$C_6H_5CH_2F$ and 4-$C_6H_4FCH_3$ will isomerize before dissociation channels open. Although α-$C_6H_5CH_2F$ and 4-$C_6H_4FCH_3$ can isomerize to one another via a six-membered to seven-membered ring isomerization path, analogous to that of toluene, certain requirements must also be satisfied in order to explain the following set of observations. These include the following: (1) Fluorine-atom elimination is the dominant channel in α-$C_6H_5CH_2F$, (2) the small translational energy distribution for HF elimination, and (3) the fast dissociation rate for α-$C_6H_5CH_2F$ compared with 4-$C_6H_4FCH_3$. The corresponding requirements include the following: (1) Fluorine atom elimination from the particular isomer must have a relatively low dissociation threshold. (2) The dissociation threshold and exit barrier for HF elimination from the isomer must be small. (3) The isomer must be easier to access from α-$C_6H_5CH_2F$ than from 4-$C_6H_4FCH_3$, because of large branching ratios for F and HF elimination from α-$C_6H_5CH_2F$ compared with that from 4-$C_6H_4FCH_3$.

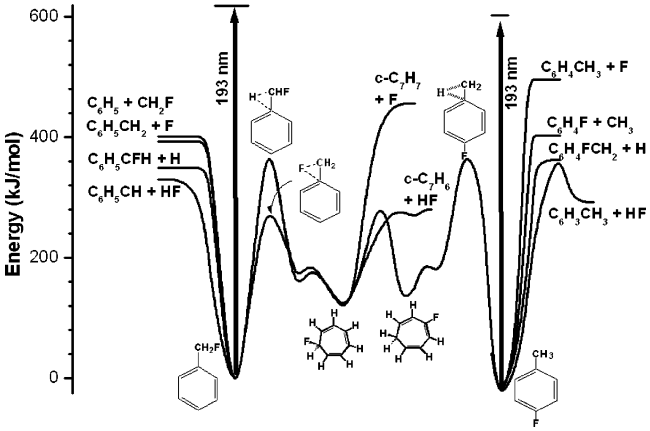

Figure 13. Potential energy diagram for various dissociation and isomerization channels of α-fluorotoluene and 4-fluorotoluene.

Figure 13 depicts the potential energies for the reactants, products, and transition states. Note that F-atom elimination from α-fluorotoluene has a lower dissociation threshold than that for C−C bond cleavage. Three-center HF elimination from the CH_2F group does not have an exit barrier, and the dissociation threshold is very low, providing one possible dissociation mechanism for HF elimination. There are two isomerization paths from the six-membered ring of α-fluorotoluene to the seven-membered ring of fluoro-cycloheptatriene. One route proceeds from 6-membered to 7-membered ring structures via H-atom migration, for which the barrier height is 364 kJ/mol (close to the value for toluene). The other isomerization path is from a six-membered to seven-membered ring through F-atom migration. In this case, the barrier height is only 260 kJ/mol. As a result, the majority of hot α-fluorotoluene molecules should isomerize to a seven-membered ring via the F-atom migration pathway, prior to dissociation.

Figure 13 also gives the potential energies for reactants, products, and transition states concerning 4-fluorotoluene. The dissociation threshold for F-atom elimination from the phenyl ring is too high for the reaction to occur. On the other hand, dissociation thresholds for H-atom elimination and C−C bond cleavage and the barrier for 4-center HF elimination are nearly the same height. There are no barriers for H-atom elimination and C−C bond cleavage, and these dissociation channels occur via a variational transition state, expected to have larger dissociation rates than that for HF elimination. Indeed, the large exit barrier height for HF elimination from 4-fluorotoluene is inconsistent with the small photofragment translational energy we observe in our experiments. Therefore, we conclude that HF elimination through the four-center mechanism does not occur. In contrast to α-fluorotoluene, the sole isomerization route from the 6-membered ring 4-fluorotoluene to the 7-membered ring fluoro-cycloheptatriene is via H-atom migration. The barrier height is close to the dissociation thresholds for the 6-membered ring. As a consequence, most of the hot 4-fluorotoluene molecules dissociate directly into fragments from the 6-membered ring through H-atom elimination and C−C bond cleavage. Only a small fraction of hot 4-fluorotoluene isomerizes from the 6-membered to the 7-membered ring. Because H-atom migration within the 7-membered ring is swift because of a low-energy barrier (as illustrated in Figure 13), a variety of 7-membered rings can isomerize into one another.

Elimination of HF from the 7-membered ring isomers is also possible. Low dissociation thresholds for HF elimination from α-fluorotoluene and the 7-membered ring isomers, in addition to the low isomerization barriers between α-fluorotoluene and 7-membered ring isomers, result in higher dissociation rates for α-fluorotoluene than for 4-fluorotoluene. However, once 4-fluorotoluene isomerizes to a 7-membered ring structure, it can quickly become α-fluorotoluene and follow the dissociation channels for α-fluorotoluene. This can explain why the minor channels for 4-fluorotoluene are major channels for α-fluorotoluene and why the major channels for 4-fluorotoluene were not observed from α-fluorotoluene.

A comparison of toluene, *m*-xylene, 4-methylpyridine, aniline, α-fluorotoluene, and 4-fluorotoluene indicates that six-membered to seven-membered ring isomerization must be a general isomerization mechanism for these aromatic molecule analogs. However, results of isomerization in aniline, 4-methylpyridine, 4-fluorotoluene, and α-fluorotoluene are quite different from those for toluene and xylene. For example, six-membered to seven-membered ring isomerization in alkyl-substituted benzenes is observed only when using isotope-labeled compounds. For non-isotope-labeled molecules, the net effect of isomerization is equivalent to that of ring permutation. For instance, with xylene, the isomerization involves the exchange of relative alkyl group positions, giving nearly the same result as ring permutation. On the other hand, methylpyridine can isomerize to aniline, and 4-fluorotoluene can transform into α-fluorotoluene via respective six-membered to seven-membered ring isomerizations. These cannot be achieved by ring permutation. It makes the six-membered ring to seven-membered ring isomerization significantly important in heterocyclic aromatic molecules. Of particular significance with this type of isomerization is that the carbon, nitrogen, fluorine, and hydrogen atoms belonging to alkyl or amino groups are involved in the exchange with atoms of the aromatic ring. However, the isomerization takes place on the ground electronic state with large vibrational energy and does not easily occur in condensed phase because of rapid vibrational relaxation.

C. Chromophores of the Amino Acid Tyrosine. Aromatic amino acids, including tyrosine, tryptophan, and histidine, have very large UV absorption cross sections. However, fluorescence quantum yields for these molecules are quite small; indicating the existence of fast nonradiative processes, efficiently quenching the fluorescence.[52−55] The nonradiative process is assumed to be ultrafast internal conversion. As internal conversion shifts electronic energy into vibrational energy, the resulting highly vibrationally excited molecules quickly dissipate their vibrational energy to surrounding molecules through intermolecular energy transfer before chemical reactions take place. This so-called photostability prevents the undesirable photochemical reactions of these molecules upon UV irradiation.

Recent ab initio calculations, point to dissociation, rather than internal conversion as the major nonradiative process quenching the fluorescence of certain amino acid chromophores.[56−60] Phenol (an amino acid chromophore of tyrosine) has a first excited $1\pi\pi^*$ state, bound with respect to O−H bond distance, and a $1\pi\sigma^*$ state, which is repulsive. The diabatic $1\pi\sigma^*$ potential correlates with ground state products, C_6H_5O + H. Although absorption of UV photons corresponds to excitation to the $1\pi\pi^*$ state, population of this state can quickly be transferred to the $1\pi\sigma^*$ potential through a conical intersection. As a result, instead of internal conversion to the ground electronic state, dissociation from $1\pi\sigma^*$ provides another viable explanation for the rapid fluorescence quenching. Similar potential energy surfaces have been found for indole and imidazole, the respective chromophores of the amino acids, tryptophan and histidine. Because dissociation from an excited state with a repulsive potential energy surface is swift, quenching is incomplete even in condensed phase. Consequently, dissociation from the repulsive state and reactions following the generation of radicals from dissociation become a potential problem in amino acid photostability.

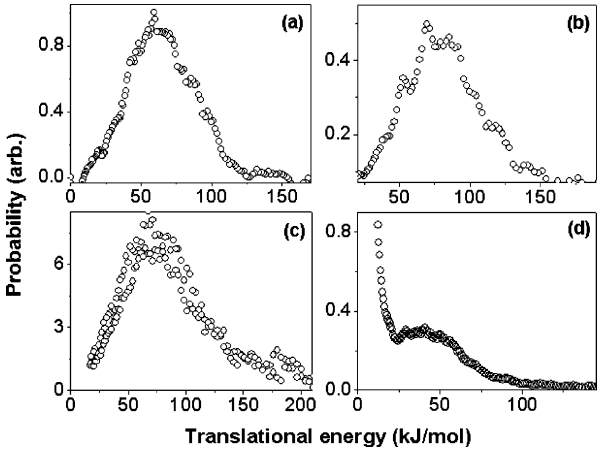

Figure 14. Photofragment translational energy at 248 nm: (a) $C_6H_5OH \rightarrow C_6H_5O + H$, (b) $CH_3C_6H_4OH \rightarrow CH_3C_6H_4O + H$, (c) $C_2H_5C_6H_4OH \rightarrow C_2H_5C_6H_4O + H$, and (d) $NH_2C_2H_4C_6H_4OH \rightarrow NH_2CH_2 + CH_2C_6H_4OH$.

Photodissociation channels and fragment translational energy distributions of phenol, *p*-methylphenol, *p*-ethylphenol, and *p*-(2-aminoethyl)phenol at 248 nm are shown in Figure 14. At 248 nm, H-atom elimination is the major dissociation channel for phenol, along with a small amount of CO elimination.[61−62] With H-atom elimination, the average translational energy release is large. The peak of the distribution is located at 58 kJ/mol. Notice that the maximum translational energy reaches nearly that of the maximum available energy for the reaction. This is characteristic of dissociation from an excited state having a repulsive potential or from an electronic state with a large exit barrier. Because formation of the phenoxy radical along with the hydrogen atom from the ground electronic state does not have a large exit barrier, the large translational energy distribution supports the dissociation mechanism from a repulsive state.

Hydrogen atom elimination is the only dissociation channel for *p*-methylphenol and *p*-ethylphenol.[63] This finding, along with translational energy distributions, which resemble those for H-atom elimination from the photodissociation of phenol, suggests a similar dissociation mechanism. Indeed, similar repulsive potential energy surfaces along the O−H bond distance of *p*-methylphenol and *p*-ethylphenol were determined from ab initio calculations.[63]

Interestingly, quite different photodissociation properties were found during the photodissociation of *p*-(2-aminoethyl)phenol.[63] No fragments corresponding to H-atom elimination were found; only C−C bond cleavage was observed. The photofragment translational energy distribution finds two components within the distribution. This includes a slow component with a small average translational energy release, and the probability decreases monotonically with translational energy. This type of behavior is characteristic of dissociation from hot molecules. There is also a fast component having a large average translational energy release and a peak for the distribution, which is located far from zero. This is typical of dissociation from an excited state with a repulsive potential energy surface or from an electronic state with a large exit barrier. Because the alkyl

group is not an electronic chromophore at 248 nm, an electronic excited state with a repulsive potential along the C−C bond is not expected to play a role in this photon energy region. The dissociation mechanism was interpreted with the slow component in the translational energy distribution resulting from ground state dissociation and the fast component resulting from triplet state dissociation. Two-component translational energy distributions resembling those for alkyl group C−C bond cleavage have been found in the photodissociation of ethylbenzene, propylbenzene, and ethyltoluene at 248 nm.[64−66]

A comparison of dissociation properties for the amino acid chromophores reveals an interesting side-chain dependence. The alkyl and amino groups for these molecules are not absorption chromophores at 248 nm. Consequently, the photoexcitation of phenol, *p*-methylphenol, *p*-ethylphenol, and *p*-(2-aminoethyl)-phenol with 248 nm photons corresponds to excitation of the phenyl ring. Decay of the excited phenyl ring differs for these molecules. For phenol, *p*-methylphenol, and *p*-ethylphenol, relaxation of the excited phenyl ring is predominantly through coupling between $\pi\pi^*$ and $\pi\sigma^*$ states. As a result, H-atom elimination from a repulsive state is the major dissociation channel. By contrast, *p*-(2-aminoethyl)phenol does not dissociate on a repulsive potential energy surface, instead dissociating through C−C bond cleavage on the ground electronic state or via a triplet state. The results suggest that it is not straightforward to predict the amino acid photochemical properties from simple chromophores.

IV. Summary

Substituents in aromatic molecules can produce surprising effects in the isomerization and dissociation properties of these molecules leading to the rich variety of aromatic photochemistry. These effects can also make precise experimental measurements more difficult to attain. Multimass ion imaging techniques provide many advantages over other methods used in translational energy spectroscopy. We offer the following summary of the method. (1) The translational energy distributions for multiple fragments are measured simultaneously in the center-of-mass frame, allowing for a straightforward analysis of the data. Multimass capability lends itself to the efficient investigation of photodissociation, especially for polyatomic molecules having multiple dissociation channels. (2) Fragment cracking during the ionization process is minimized because of the low VUV photon energies used. Fragment cracking becomes especially problematic when different fragments produce identical daughter ions. This can happen even for medium-sized (>10 atoms) polyatomic hydrocarbons when electron impact ionization is the method of choice. Decreasing the percentage for fragment cracking not only simplifies data analysis but also enhances the signal-to-noise (S/N) ratio. (3) Dissociation channels can be investigated without interference, for example, from dissociation caused by the probe laser. For certain polyatomic molecules, dissociation rates can be as slow as several hundred microseconds. Molecules that have obtained large amounts of energy without dissociating into fragments immediately will dissociate into smaller neutral and ionic fragments if exposed to the probe laser. Conventional pump−probe experiments that utilize a delay time between the pump and the probe laser, which is shorter than the dissociation lifetime for the molecule, set the stage for dissociation of the molecule by the probe laser, thereby generating a large interference. (4) The high detection sensitivity of our method allows us to study photodissociation processes under low photolysis laser fluence. As a result, one-photon and two-photon dissociations can easily be distinguished from one another. Additionally, molecules having a low vapor pressure can be investigated in tandem with a molecular beam. (5) The range for measured dissociation rates is large. It is from 10^8 to 10^4 s^{-1}. These advantages become particularly important in photodissociation studies of large molecules like aromatic molecules with multiple dissociation channels and slow dissociation rates. Future challenges will encompass the study of other important aromatic molecules, including amino acids and nucleic acids.

Acknowledgment. This work was supported by the National Science Council Taiwan under Contract No. NSC 95-2113-M-001-051.

References and Notes

(1) Wodtke, A. M.; Lee, Y. T. High resolution photofragmentation-Translational Spectroscopy. In *Molecular Photodissociation Dynamics*; Ashfold, M. N. R., Baggott, J. E., Eds.; Royal Society of Chemistry: London, 1987.

(2) Tsai, S. T.; Lin, C. K.; Lee, Y. T.; Ni, C. K. *Rev. Sci. Instrum.* **2001**, *72*, 1963.

(3) Huang, C. L.; Lee, Y. T.; Ni, C. K. Multimass ion imaging, A new experimental technique and the application in photodissociation of small aromatic molecules. In *Modern Trends in Chemical Reaction dynamics: Experiment and Theory (Part II);* Liu, K., Yang, X., Eds.; World Scientific: River Edge, NJ, 2004.

(4) Ni, C. K.; Lee, Y. T. *Int. Rev. Phys. Chem.* **2004**, *23*, 187.

(5) Foote, J. K.; Mallon, M. H.; Pitts, J. N., Jr. *J. Am. Chem. Soc.* **1966**, *88*, 3698.

(6) Shindo, K.; Lipsky, D. *J. Chem . Phys.* **1966**, *45*, 2292.

(7) Ward, H. R.; Wishnok, J. S.; Sherman, P. D., Jr. *J. Am. Chem. Soc.* **1967**, *89*, 162.

(8) Kaplan, L.; Wilzbach, K. E. *J. Am. Chem. Soc.* **1967**, *89*, 1030.

(9) Kaplan, L.; Walch, S. P.; Wilzbach, K. E. *J. Am. Chem. Soc.* **1968**, *90*, 5646.

(10) Ward, H. R.; Wishnok, J. S. *J. Am. Chem. Soc.* **1968**, *90*, 5353.

(11) Mellows, F.; Lipsky, S. *J. Phys. Chem.* **1966**, *70*, 4076.

(12) Yokoyama, A.; Zhao, X.; Hintsa, E. J.; Continetti, R. E.; Lee, Y. T. *J. Chem. Phys.* **1990**, *92*, 4222.

(13) Mebel, A. M.; Lin, S. H.; Yang, X. M.; Lee, Y. T. *J. Phys. Chem.* **1997**, *101*, 6781.

(14) Mebel, A. M.; Lin, M. C.; Chakraborty, D.; Park, J.; Lin, S. H.; Lee, Y. T. *J. Chem. Phys.* **2001**, *114*, 8421.

(15) Kislov, V. V.; Nguyen, T. L.; Mebel, A. M.; Lin, S. H.; Smith, S. C. *J. Chem. Phys.* **2004**, *120*, 7008.

(16) Tsai, S. T.; Lin, C. K.; Lee, Y. T.; Ni, C. K. *J. Chem. Phys.* **2000**, *113*, 67.

(17) Tsai, S. T.; Huang, C. L.; Lee, Y. T.; Ni, C. K. *J. Chem. Phys.* **2001**, *115*, 2449.

(18) Linnell, R. H.; Noyes, W. A. *J. Am. Chem. Soc.* **1951**, *73*, 3986.

(19) Price, D.; Rtajczak, E. *J. C. S. Chem. Commun.* **1976**, *22*, 902.

(20) Prather, K. A.; Lee, Y. T. *Israel J. Chem.* **1994**, *34*, 43.

(21) Lin, M. F.; Dyakov, Y. A.; Tseng, C. M.; Mebel, A. M.; Lin, S. H.; Lee, Y. T.; Ni, C. K. *J. Chem. Phys.* **2005**, *123*, 054309.

(22) Pickett, L. W.; Corning, M. E.; Wieder, G. M.; Semenow, D. A.; Buckeley, J. M. *J. Am. Chem. Soc.* **1953**, *75*, 1618.

(23) Wilzbach, K. E.; Rausch, D. J. *J. Am. Chem. Soc.* **1970**, *92*, 2178.

(24) Caplain, S.; Lablache-Combier, A. *Chem. Commun.* **1970**, 1247.

(25) Johnson, D. W.; Austel, V.; Feld, R. S.; Lemal, D. M. *J. Am. Chem. Soc.* **1970**, *92*, 7505.

(26) Lahmani, F.; Ivanoff, N. *J. Phys. Chem.* **1972**, *76*, 2245.

(27) Lin, M. F.; Dyakov, Y. A.; Tseng, C. M.; Mebel, A. M.; Lin, S. H.; Lee, Y. T.; Ni, C. K. *J. Chem. Phys.* **2006**, *124*, 084303.

(28) Gregory, T.; Hirayama, A. F.; Lipsky S. *J. Chem. Phys.* **1973**, *58*, 4697.

(29) Burgstahler, A. W.; Chien, P. L. *J. Am. Chem. Soc.* **1964**, *86*, 2940.

(30) Kaplan, L.; Wilzbach, K. E.; Brown, W. G.; Yang, S. S. *J. Am. Chem. Soc.* **1965**, *87*, 675.

(31) Wilzbach, K. E.; Kaplan, L. *J. Am. Chem. Soc.*, **1965**, *87*, 4004; **1964**, *86*, 2307.

(32) Besten, I. E. D.; Kaplan, L.; Wilzbach, K. E. *J. Am. Chem. Soc.* **1968**, *90*, 5868.

(33) Bryce-Smith, D.; Gilbert, A. In *Rearrangement in Ground and Excited States;* De Mayo, P., Ed.; Academic Press: New York, 1980; Vol. 3.

(34) Jackson, A. H.; Kenner, G. W.; McGillvray, G.; Sach, G. S. *J. Am. Chem. Soc.* **1965**, *87*, 675.

(35) Wilzbach, K. E.; Harkness, A. L.; Kaplan, L. *J. Am. Chem. Soc.* **1968**, *90*, 1116.

(36) Hippler, H.; Schubert, V.; Troe, J.; Wendelken, H. *J. Chem. Phys. Lett.* **1981**, *84*, 253.
(37) Park, J.; Bersohn, R.; Oref, I. *J. Chem. Phys.* **1990**, *93*, 5700.
(38) Fröchtenicht, R. *J. Chem. Phys.* **1994**, *102*, 4850.
(39) Nakashima, N.; Yoshihara, K. *J. Phys. Chem.* **1989**, *93*, 7763.
(40) Luther, K.; Troe, J.; Weitzel, K. L. *J. Phys. Chem.* **1990**, *94*, 6316.
(41) Brand, U.; Hippler, H.; Lindemann, L.; Troe, J. *J. Phys. Chem.* **1990**, *94*, 6305.
(42) Shimada, T.; Ojima, Y.; Nakashima, N.; Izawa, Y.; Yamanaka, C. *J. Phys. Chem.* **1992**, *96*, 6298.
(43) Lin, C. K.; Huang, C. L.; Jiang, J. C.; Chang, H.; Lin, S. H.; Lee, Y. T.; Ni, C. K. *J. Am. Chem. Soc.* **2002**, *124*, 4068.
(44) Huang, C. L.; Jiang, J. C.; Lee, Y. T.; Ni, C. K. *J. Phys. Chem. A* **2003**, *107*, 4019.
(45) Tseng, C. M.; Dyakov, Y. A.; Huang, C. L.; Mebel, A. M.; Lin, S. H.; Lee, Y. T.; Ni, C. K. *J. Am. Chem. Soc.* **2004**, *126*, 8760.
(46) Biesner, J.; Schnieder, L.; Ahlers, G.; Xie, X.; Welge, K. H.; Ashfold, M. N. R.; Dixon, R. N. *J. Chem. Phys.* **1989**, *91*, 2901.
(47) Waschewsky, G. C. G.; Kitchen, D. C.; Browning, P. W.; Butler, L. J.; *J. Phys. Chem.* **1995**, *99*, 2635.
(48) Forde, N. R.; Morton, M. L.; Curry, S. L.; Wrenn, S. J.; Butler, L. J. *J. Chem. Phys.* **1999**, *111*, 4558.
(49) Huang, C. L.; Jiang, J. C.; Dyakov, Y. A.; Lin, M. F.; Tseng, C. M.; Lin, S. H.; Lee, Y. T.; Ni, C. K. *J. Chem. Phys.* **2006**, *125*, 133305.
(50) Huang, C. L.; Jiang, J. C.; Mebel, A. M.; Lee, Y. T.; Ni, C. K. *J. Chem. Phys.* **2005**, *125*, 9814.
(51) Lin, M. F.; Dyakov, Y. A.; Lin, S. H.; Lee, Y. T.; Ni, C. K. *J. Phys. Chem. B* **2005**, *109*, 8344. Robin, M. B. *Higher Excited States of Polyatomic Molecules*; Academic Press: New York, 1972.
(52) Robin, M. B. *Higher Excited States of Polyatomic Molecules*; Academic Press: New York, 1972.
(53) Callis, P. R. *Annu. Rev. Phys. Chem.* **1983**, *34*, 329.
(54) Creed, D. *Photochem. Photobiol.* **1984**, *39*, 537.
(55) Crespo-Hernandez, C. E.; Cohen, B.; Hare, P. M.; Kohler, B. *Chem. Rev.* **1977**, *104*, 2004.
(56) Sobolewski, A. L.; Domcke, W. *Chem. Phys.* **2000**, *259*, 181.
(57) Sobolewski, A. L.; Domcke, W. *J. Phys. Chem. A* **2001**, *105*, 9275.
(58) Sobolewski, A. L.; Domcke, W.; Dedonder-Lardeux, C.; Jouvet, C. *Phys. Chem. Chem. Phys.* **2002**, *4*, 1093.
(59) Roos, B. O.; Malmqvist, P. A.; Molina, V.; Serrano-Andres, L.; Merchan, M. *J. Chem. Phys.* **2002**, *116*, 7526.
(60) Lan, Z. G.; Domcke, W.; Vallet, V.; Sobolewski, A. L.; Mahapatra, S. *J. Chem. Phys.* **2005**, *122*, 224315.
(61) Tseng, C. M.; Lee, Y. T.; Ni, C. K. *J. Chem. Phys.* **2004**, *121*, 2459.
(62) Tseng, C. M.; Lee, Y. T.; Lin, M. F.; Ni, C. K.; Liu, S. Y.; Lee, Y. P.; Xu, Z. F.; Lin, M. C. *J. Phys. Chem. A*, submitted.
(63) Tseng, C. M.; Lee, Y. T.; Ni, C. K.; Chang, J. L. *J. Phys. Chem. A* **2007**, *111*, 6674.
(64) Huang, C. L.; Jiang, J. C.; Lin, S. H.; Lee, Y. T.; Ni, C. K. *J. Chem. Phys.* **2002**, *116*, 7779.
(65) Huang, C. L.; Jiang, J. C.; Lin, S. H.; Lee, Y. T.; Ni, C. K. *J. Chem. Phys.* **2002**, *117*, 7034.
(66) Huang, C. L.; Dyakov, Y. A.; Lin, S. H.; Lee, Y. T.; Ni, C. K. *J. Phys. Chem. A* **2005**, *109*, 4995.